

# Failure mode engineered high-energy-absorption metamaterials with biomimetic hierarchical microstructures and artificial grain boundaries

**Zhenyang Gao**

Shanghai Jiao Tong University

**Hua Sun**

Shanghai Jiao Tong University

**Hongze Wang** (✉ [hz.wang@sjtu.edu.cn](mailto:hz.wang@sjtu.edu.cn))

Shanghai Jiao Tong University

**Yi Wu**

Shanghai Jiao Tong University

**Tengteng Sun**

Shanghai Jiao Tong University

**Haowei Wang**

Shanghai Jiao Tong University

---

## Article

**Keywords:** additive manufacturing, metamaterials, bio-inspired, energy absorption, spherical hollow structures

**Posted Date:** October 28th, 2021

**DOI:** <https://doi.org/10.21203/rs.3.rs-1003421/v1>

**License:** © ⓘ This work is licensed under a Creative Commons Attribution 4.0 International License.

[Read Full License](#)

---

# **Failure mode engineered high-energy-absorption metamaterials with biomimetic hierarchical microstructures and artificial grain boundaries**

Keywords: additive manufacturing, metamaterials, bio-inspired, energy absorption, spherical hollow structures

## **Abstract**

For numerous engineering applications, there is a high demand for protective lightweight structures with outstanding energy absorption performance and the ability to prevent catastrophic structural failures. In nature, most species have evolved with hierarchical biological structures that possess novel mechanical properties, including ultrahigh specific energy absorption, progressive laminated failure modes, and ability for crack arrestment, in order to defend themselves from hostile environments. In this study, a novel protective metamaterial having spherical hollow structures (SHSs) was developed with different hierarchical microstructures. An artificial failure mode engineering strategy was proposed by tailoring the microstructures of SHS unit cells. To demonstrate the effectiveness of the proposed method, a composite hierarchical SHS lattice structure was developed using a biomimetic laminated failure mode and through a hardening mechanism, mimicking crystal grain boundaries. The quasi-static compressive results indicated a significant improvement in the specific energy absorption, an enhanced plateau stress magnitude, and an obvious delay in the densification stage for the composite hierarchical SHS lattice owing to the constraining effect of its mesoscale grain boundaries and an increased number of intensively engineered laminated failure levels. This novel type of metamaterial was shown to be immensely beneficial in designing lightweight protective aerospace components such as turbine blade lattice infills.

## **Introduction**

Metamaterials are artificially engineered materials with complicated microstructures designed to possess novel properties such as a high stiffness-to-weight ratio<sup>[1]</sup>, a negative Poisson's ratio<sup>[2]</sup>, improved fracture resistance<sup>[3, 4]</sup>, improved damage tolerance<sup>[5]</sup>, vibration migration<sup>[6]</sup>,

and enhanced specific energy absorption<sup>[7, 8]</sup>. Among the different metamaterial structural designs, the spherical hollow structure (SHS) exhibits tremendous energy absorption and impact resistance capabilities and is lightweight because of the high porosity and highly plastic behavior of its microstructure. Numerous studies have been conducted to demonstrate the energy absorption advantages and potential applications of SHSs. Gao et al.<sup>[9]</sup> experimentally characterized the mechanical behavior of metallic hollow sphere (MHS) materials. In their work, the stress–strain curve of a typical MHS foam showed three phases: (1) the elastic phase, (2) the plateau phase, and (3) the densification phase, wherein the wide range of the plateau phase was found to be the main source of its superior energy absorption capability. Song et al.<sup>[10]</sup> discussed the energy absorption properties of an MHS material under impact loading. Their research indicates that the MHS is an effective protective material to shield bridge piers against vehicle impact. To further explore the relationship between the energy absorption behavior and the design parameters of SHS materials, the mechanical properties of SHS were studied with different sphere sizes, packing patterns, and relative densities. To investigate the compressive energy absorption responses of the adhesively bonded hollow steel spheres, steel foams with two different sphere sizes were fabricated by Yiatros et al.<sup>[11]</sup>. The experimental results revealed that the steel foam with smaller spheres possessed a higher energy absorption value and plateau stress. Yu et al.<sup>[12]</sup> studied the fundamental mechanical characteristics and energy absorption capacity (EAC) of MHSs through experimental, numerical, and analytical approaches. The quasi-static and dynamic compression experimental results indicated significant strain hardening phenomena and an obvious dynamic effect. Empirical functions have been established between the elastic modulus, yield strength, plateau stress, and relative density for the face-centered-cubic-(FCC)-packed MHSs, while analytical relations were derived for the yield strength, EAC, and strain hardening behavior at different relative densities. Nevertheless, the SHS structures proposed in these studies were manufactured with identical hollow spheres, wherein the structure of the SHS was not optimized to further improve its

energy absorption potential. Thus, several innovative composite design features have been recently proposed to enhance the energy absorption and impact performance of SHS structures. Li et al.<sup>[13]</sup> developed a novel hybrid structure by assembling the MHSs into the tetrahedra and octahedra of the inner spaces of the wire-woven bulk kagome (WBK). It was found that the buckling effect of the WBK structure was resisted by including MHSs, where improved stiffness, strength, and energy absorption values were observed. The high-strain-rate compressive responses of Al380-Al<sub>2</sub>O<sub>3</sub> hollow spheres with different sphere sizes and size distributions were studied by Maria et al.<sup>[14]</sup>. In their study, a higher peak strength, plateau strength, and toughness of the hollow sphere foams were observed for foams containing spheres with a larger thickness-to-diameter ratio. Liu et al.<sup>[15]</sup> proposed a density grade thin-walled design for MHS arrays to improve the dynamic properties of cellular materials. Consequently, the transformation of the MHS packing pattern was observed. It was also found that the gradient profile of the MHS arrays generated higher energy absorption value against high impact velocities. However, these hollow spheres are usually formed through traditional powder metallurgy techniques and are connected based on conventional bonding methods, such as sintering<sup>[16]</sup> and adhesive bonding<sup>[17]</sup>. Typically, these conventional manufacturing methods lead to a poorly controlled microstructure, limited design potential, and reduced SHS mechanical response owing to their fabrication limits.

Nevertheless, the maturing additive manufacturing (AM) technology now allows researchers to develop materials with more precisely controlled microstructures without a significant increase in the manufacturing cost<sup>[18]</sup>. For instance, a spherical body-centered-cubic-(BCC)-shell composite lattice structure were 3D-printed by Yuan et al.<sup>[19]</sup> with carbon nanotube reinforced polyimide (CNT/PA12). Compared with traditional elastomer foams, a higher energy absorption value and a larger energy absorption scale factor with different lattice densities were obtained. Dai et al.<sup>[20]</sup> proposed and fabricated hollow sphere structures with perforations (PHSSs) in simple cubic (SC), BCC, and FCC packing arrangements through

selective laser melting (SLM). The results of the uniaxial compressive tests revealed that the specific energy absorption and strength of the additively manufactured PHSSs outperformed the traditional MHSs. It was also observed that the large deformation and EAC of PHSSs are sensitive to the geometric design parameters, including the wall thickness, hole diameter, and sphere arrangement. To improve the damage tolerance of additively manufactured ceramic materials, Sajadi et al.<sup>[21]</sup> 3D-printed spherical architected structures with silica-filled preceramic polymers and coated the surface of the spherical lattice with a flexible epoxy polymer. The proposed surface modification technique has proved to be effective in improving the damage tolerance of ceramic-based composite SHS lattices compared to their counterparts. Some researchers have further utilized the design complexity offered by AM to develop lattice structures with artificially distributed non-uniform microstructures to further promote their functional performance. For example, Alonso et al.<sup>[5]</sup> proposed an innovative distribution of lattice microstructures mimicking the hardening strategies of crystals to improve the overall damage tolerance of lattice materials. In their research, the artificially designed grain boundary effectively prevented cracks from propagating across it in the overall lattice structures. Inspired by the crack deflection of wood sap channels, Manno et al. pre-engineered multiple vertical crack paths in 2D honeycomb lattice structures by varying the relative density of the microstructural honeycomb cells<sup>[22]</sup>. Based on the finite element analysis (FEA) results, the 2D honeycomb lattice with a bio-inspired crack path significantly increased its fracture energy. Gao et al.<sup>[3]</sup> engineered the crack path of octet-truss lattice structures by optically programming the distribution of the mechanical properties of resin materials. As a result, a 152% increase in fracture energy was observed for the optically programmed octet-truss lattice structures compared to that achieved by their conventionally manufactured counterparts without pre-engineered crack paths. For SHS lattice structures, however, limited research efforts have been devoted toward the design of an effective energy-absorbing SHS lattice structure with an artificially engineered improvement of its mechanical performance by varying its

microstructures. To achieve this novel energy absorbing SHS design, however, the development of a spherical lattice surface that is smoothly connected to the lattice structure, with varying mechanical properties in different lattice regions, remains a challenge.

Moreover, most biological structures have evolved with interesting macroscopic distributions of hierarchical microstructures to achieve excellent mechanical performance. These features effectively increase survivability in severe natural environments and thus act as a valuable design database for material scientists. For example, Sadeghzade et al.<sup>[4]</sup> mimicked the hierarchical microstructure of spicule structures to develop novel crack-deflecting circular structures. Their results indicated that the spicule-inspired design strategy improves both the strength and flexibility of the cylindrical structure. Gu et al.<sup>[23]</sup> investigated the fracture toughness of brick-and-mortar composite structures with respect to the volume fraction of their stiff and soft components and the number of mineral bridges. To improve the fracture toughness of the material, it is recommended by their work to increase the fraction of the soft components until the maximum value of the fracture toughness is reached, while the presence of mineral bridges is shown to be effective in deflecting cracks in the material. A crack-arresting material was also proposed by Gu et al.<sup>[24]</sup>. This material mimics the hierarchical structures of the conch-shell, which itself possesses alternating sheets of mineralized calcium carbonate structures separated by organic layers. Their results revealed that the catastrophic failure mode of the structure can be prevented by increasing the number of hierarchical levels. Meza et al.<sup>[25]</sup> studied the mechanical robustness and damage tolerance of hierarchically designed nano-lattices with three orders of octahedron hierarchical structures, wherein the combinations of solid polymers, hollow ceramics, and polymer/ceramic composites were compared. It was found that an appropriate hierarchical design of the microstructures can efficiently distribute the load over each region of the entire structure. Therefore, designing a bio-inspired SHS (BH-SHS) metamaterial with hierarchical topologies and proposing an effective failure mode engineering method for BH-SHS materials based on the use of artificially alternated lattice

microstructures is a promising approach for the development of next-generation protective SHS metamaterials.

In this work, the SHS lattice structures were tailored with artificially distributed biomimetic hierarchical topologies, and a significant improvement in the specific energy absorption was observed for the composite SHS lattice structures with the pre-engineered biometric laminated failure mode and crystal-inspired mesoscale grain boundaries. Specifically, the design and modeling methods proposed in Section 2 were based on simulation and experimental efforts to develop biometric hierarchical SHS (BH-SHS) unit cells and engineer the failure mode of BH-SHS lattice structures, wherein two types of hierarchical topology were applied: (1) a stretch-dominated honeycomb (SHC) and (2) a bending-dominated honeycomb (BHC). Section 3 details the experiments that were performed to study the effects of the gradient magnitude for SHC-SHS and BHC-SHS lattice structures with a pre-engineered layer-wise failure sequence, wherein two types of hierarchical topologies with optimal gradient levels were combined to form a composite SHS lattice structure with artificially engineered grain boundaries. The failure mechanisms of the proposed lattice structures were characterized on the basis of the experimental deformation results, while the normalized average plateau stress, densification strain, specific energy absorption, and specific strength were derived and analyzed on the basis of the stress–strain curves. At the end of the paper, the conclusions are presented, and future research potentials are pointed out.

## **Results**

In this study, the SHC-SHS, BHC-SHS, and CHC-SHS lattice structures with pre-engineered failure modes were manufactured by the SLM technique using AlMgScZr powders, and quasi-static compression tests were performed to examine the mechanical responses of these samples at a compressive rate of 2 mm/min. The compositions of the powders are shown in Figure S1 and summarized in Table S2. The compressive stress–strain curves and failure propagation diagrams of the printed lattice samples are presented in Figure 1, where the experimental

recodings together with progressing stress-strain curves are delivered in Video S3 to Video S7. The quasi-static compressive behaviors and failure mechanisms were first derived for the BHC-SHS and SHC-SHS lattice structures with two distinct levels of the  $\sigma_{If}(N)$  gradients. Subsequently, a CHC-SHS lattice structure was developed through a crystal-inspired hardening distribution strategy of different unit cell topologies and a biometric laminated failure mode design with an optimal gradient of  $\sigma_{If}(N)$ , on the basis of the experimental results of the BHC-SHS and SHC-SHS gradient lattice structures. The compressive test results of the gradient BHC-SHS (BHC-G1/2) and SHC-SHS (SHC-G1/2) lattice structures are summarized in Figure 1a-b, wherein G1 has a larger level of  $\sigma_{If}(N)$  gradient than G2. Similar to the compressive behavior of the BH-SHS unit cells, the stress–strain curves of the BHC-G1/2 and SHC-G1/2 lattice structures could be characterized into three different stages:

- I: The wavy stage was composed of the first ( $I_1$ ) and secondary ( $I_2$ ) sub-wavy stages, wherein a significant fluctuation of stress was observed.
- II: The climbing plateau stage, wherein a steady development of the stress was observed.
- III: The densification stage, wherein the structures of the lattice were forced into contact, and an exponential increase in the stress resulted.

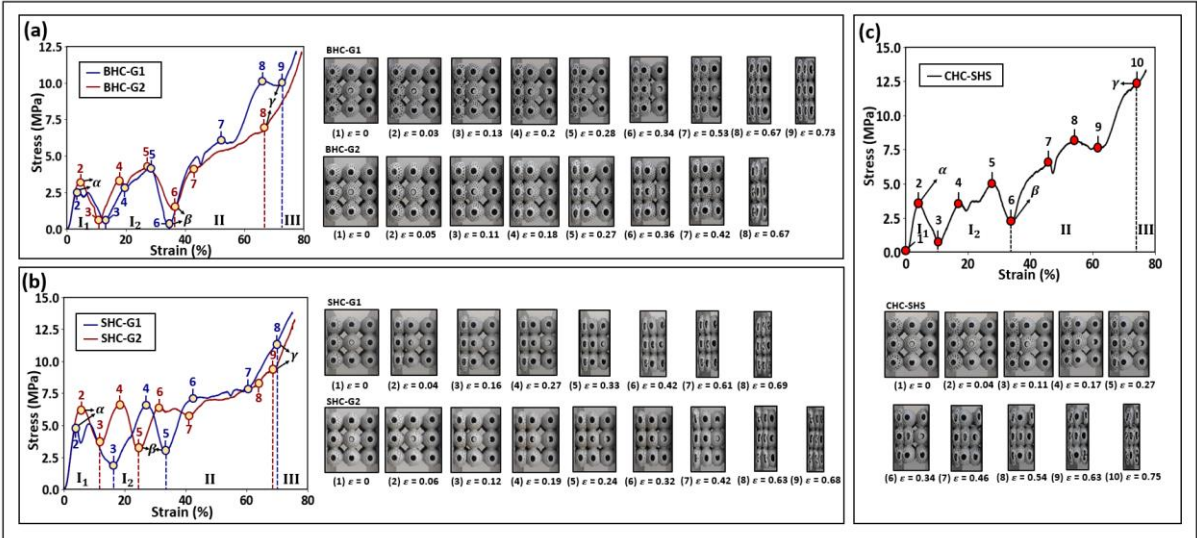


**Figure 1.** Compressive stress–strain curves for the BHC-SHS, SHC-SHS, and CHC-SHS lattice structures with pre-engineered failure modes: (a) compressive stress–strain curves and failure propagation of the BHC-G1 and BHC-G2 lattice structures; (b) compressive stress–strain

curves and failure propagation of the SHC-G1 and SHC-G2 lattice structures; and (c) compressive stress–strain curves and failure propagation of the CHC lattice structure.

Compared to the SHC-G1/2 lattice structure, a lower stress in the wavy stage and a swifter increment of the plateau stage were observed for the BHC-G1/2 lattice structure. Specifically, the values of the normalized average plateau stress ( $\sigma_{NP}$ ) for the BHC-G1 and BHC-G2 lattice structures were 2.1 MPa/MPa and 1.3 MPa/MPa, respectively, while the  $\sigma_{NP}$  values for the SHC-G1 and SHC-G2 lattice structures were 1.4 MPa/MPa and 1.0 MPa/MPa, respectively. This difference in the relative magnitude of the stress plateau was caused by the distinctive deformation mechanisms of the BHC and SHC cell topologies. As observed in the unit cell mechanical tests, the SHC-SHS unit cell exhibited higher stiffness and strength values in the wavy stage than the BHC-SHS unit cell owing to its stretch-dominated structural design. For the same topology with different gradient levels, the experimental results indicated that the lattice structure with a larger  $\sigma_{If}(N)$  gradient exhibited higher average plateau stress  $\sigma_{NP}$ , delayed densification strain  $\varepsilon_\gamma$ , and improved SEA, wherefor the specific energy calculated in Equation (16) is defined as the energy absorbed until the densification strain of the lattice structure per unit mass:

$$SEA = \frac{\int_0^{\varepsilon_\gamma} \sigma(\varepsilon) d\varepsilon}{M_{lattice}} \quad (16)$$

where  $M_{lattice}$  is the weight of the lattice structure. For instance, the  $\sigma_{NP}$ ,  $\varepsilon_\gamma$ , and SEA for the BHC-G1 lattice structure are 2.1 MPa/MPa, 73%, and 13.3 J/g, respectively, which are 55%, 9%, and 35% higher, respectively, than those of the BHC-G2 lattice structure. For the SHC-G1/2 lattice structure, the values of  $\sigma_{NP} = 1.4$  MPa/MPa,  $\varepsilon_\gamma = 69\%$ , and  $SEA = 13.81$  J/g were observed for the SHC-G1 lattice structure, which were 40%, 2%, and 1% higher, respectively, than those for the SHC-G2 lattice structure. To explore the detailed mechanisms that confer the BHC-G1 and SHC-G1 lattice structures with superior energy absorption behavior, the compressive stages of each type of unit cell within the lattice structures at critical strain values

are shown in Figure 1a-b. The compressive stages of each unit cell were derived according to the experimental failure propagation results and the mechanical modeling of the BH-SHS unit cells. The results summarized in Table S5 reveal that a reduced overlap of the failure stages between the unit cells with adjacent failure levels was provided by a larger  $\sigma_{If}(N)$  gradient in the BHC-SHS and SHC-SHS lattice structures, wherein a larger portion of the wavy stages of the unit cells contributed to the plateau phase of the resulting lattice structures. This phenomenon led to delayed structural densification and an increased normalized average plateau stress, which resulted in an improved SEA. For instance, the BHC-G2 lattice structure experienced an overlapped first wavy stage, secondary wavy stage, plateau stage, and plateau-to-densification stage of the BHC212 and BHC252 unit cells in the strain ranges of  $\varepsilon = 0.18-0.27$ ,  $\varepsilon = 0.25-0.36$ ,  $\varepsilon = 0.36-0.42$ , and  $\varepsilon = 0.42-0.67$ , respectively, while no overlap was observed prior to the densification stage of each type of unit cell for the BHC-G1 lattice. For the SHC-G1 lattice structure, two stage overlaps were found for its unit cells: (1) SHC320 and SHC420 at  $\varepsilon = 0.33-0.42$ ; and (2) SHC180, SHC320, and SHC420 at  $\varepsilon = 0.27-0.33$ . For the unit cells of the SHC-G2 lattice structures, three overlaps were found: (1) SHC260 and SHC320 at  $\varepsilon = 0.24-0.32$ ; (2) SHC260, SHC320, and SHC380 at  $\varepsilon = 0.32-0.42$ ; and (3) SHC320 and SHC380 at  $\varepsilon = 0.42-0.63$ .

Based on these analyses, the CHC-SHS lattice structure was engineered to possess solid-hardening layer-wise composition of the unit cells from the BHC-G1 and SHC-G1 lattice structures for an optimal  $\sigma_{If}(N)$  gradient; a detailed design diagram of this is shown in Figure 5c. According to the compressive test results shown in Figure 1c, a significant improvement in the stress magnitude for the plateau stage and a noticeable delay in the densification strain are obtained. Table S6 lists the corresponding compressive stages for each type of unit cell of the CHC-SHS lattice structure during compression. The results indicated that an increased number of failure levels was observed for the CHC-SHS lattice structure because of the combination of

two unit-cell topologies with different failure mechanisms. Moreover, it was observed that the constraining effects between the boundaries of different cell topologies shifted the failure sequence of the SHC-SHS unit cells earlier such that a greater stress magnitude occurred during the plateau stage of the CHC-SHS lattice structure. Quantitatively, the CHC-SHS lattice entered 10 sub-stages before densification, wherein  $\sigma_{NP} = 2 \text{ MPa/MPa}$  and  $\varepsilon_\gamma = 0.75$  were obtained. To further evaluate the mechanical performance of the BHC-G1/2, SHC-G1/2, and CHC-SHS lattice structures, the normalized average plateau stress, densification strain, specific strength, and SEA were derived (Figure 2a-b), whose specific strength (SS) is calculated using Equation (17):

$$SS = \frac{\sigma_{If}}{\rho} \quad (17)$$

where  $\rho$  is the density of the lattice structure. It was found that the CHC-SHS lattice had an increased SEA value of 15.25 J/g, which was 10.4% higher than that of the SHC-G1 lattice and 14.3% higher than that of the BHC-G1 lattice. This was due to the fact that the CHC-SHS lattice possessed a higher normalized average stress plateau and a higher densification strain than the BHC-G1/2 and SHC-G1/2 lattice structures. Similar to the BHC-G1/2 lattice structures, the CHC-SHS lattice structure could preserve a low specific strength, which made it an ideal energy absorber for components that cannot withstand high stress. Theoretical derivations were performed to understand this phenomenon. Within the CHC-SHS lattice structure, the soft BHC-SHS unit cells were inserted between stiff grains formed by the SHC-SHS unit cells, so that the stiffness and resulting strength of the structure were reduced by the rule-of-mixture and the Reuss model. According to the rule-of-mixture and the deformation stages of the unit cells, the strength of the CHC-SHS lattice at  $\varepsilon = \varepsilon_2$  can be modeled using Equations (18)–(21):

$$E_{CHC,F1} = \frac{5}{9}E_{BHC132} + \frac{4}{9}E_{SHC180} \quad (18)$$

$$E_{CHC,F2} = \frac{4}{9}E_{BHC212} + \frac{5}{9}E_{SHC320} \quad (19)$$

$$E_{CHC,F3} = \frac{5}{9}E_{BHC282} + \frac{4}{9}E_{SHC420} \quad (20)$$

$$\sigma_{CHC\alpha} = \frac{3E_{F1}E_{F2}E_{F3}}{E_{F1}E_{F2}+E_{F2}E_{F3}+E_{F1}E_{F3}} \varepsilon_2 \quad (21)$$

where  $E_{CHC,F1}$ ,  $E_{CHC,F2}$ , and  $E_{CHC,F3}$  are the effective moduli of the  $F1$ ,  $F2$ , and  $F3$  lattice layers, respectively;  $E_{BHC132}$ ,  $E_{BHC212}$ ,  $E_{BHC282}$ ,  $E_{SHC180}$ ,  $E_{SHC320}$ , and  $E_{SHC420}$  are the moduli of the BHC132, BHC212, BHC282, SHC180, SHC320, and SHC420 unit cells calculated by Equation (9), respectively; and  $\sigma_{CHC\alpha}$  is the strength of the first wavy stage for the CHC-SHS lattice. Based on Equations (18)–(21), the modulus of each CHC lattice layer was found to be decreased by the moduli of the BHC132, BHC212, and BHC282 unit cells, whereas it was estimated by the Reuss model that a further reduction in the lattice strength originated from the tandem connection of the lattice layers. For a direct comparison between the results of this work and those of the recent publications related to lightweight structures, including aluminum alloy foams, aluminum alloy lattice structures, and different SHS designs, the corresponding SEA, density-normalized plateau stress, densification strain, and density data are summarized in Ashby charts (Figure 2c-e). The results indicated that the CHC-SHS structure exhibited higher SEA, higher density-normalized plateau stress, and better deformation capability compared to the recently reported lightweight aluminum alloy structures and various SHS designs. For instance, the CHC-SHS structure possessed an SEA of 15.5 J/g and density-normalized plateau stress of 33 MPa·cm<sup>3</sup>/g, which was 72% and 50% greater, respectively, than that of the aluminum alloy lattice structures. For the perforated SHS with large deformation before densification, its SEA at  $\varepsilon_\gamma=0.75$  was still 35% lower than that of the CHC-SHS lattice structure. More generally, the CHC-SHS structure exhibited a considerably higher SEA than all summarized lightweight structures fabricated using the aluminum alloy and different SHS designs within the density range of 0–1000 kg/m<sup>3</sup>, while being capable of maintaining a low density value of 215 kg/m<sup>3</sup>. The outstanding SEA performance, deformation capability, and plateau stress of the CHC-SHS structure were attributed to its bio-inspired laminated failure mode and the crystal-inspired grain boundary hardening mechanism.

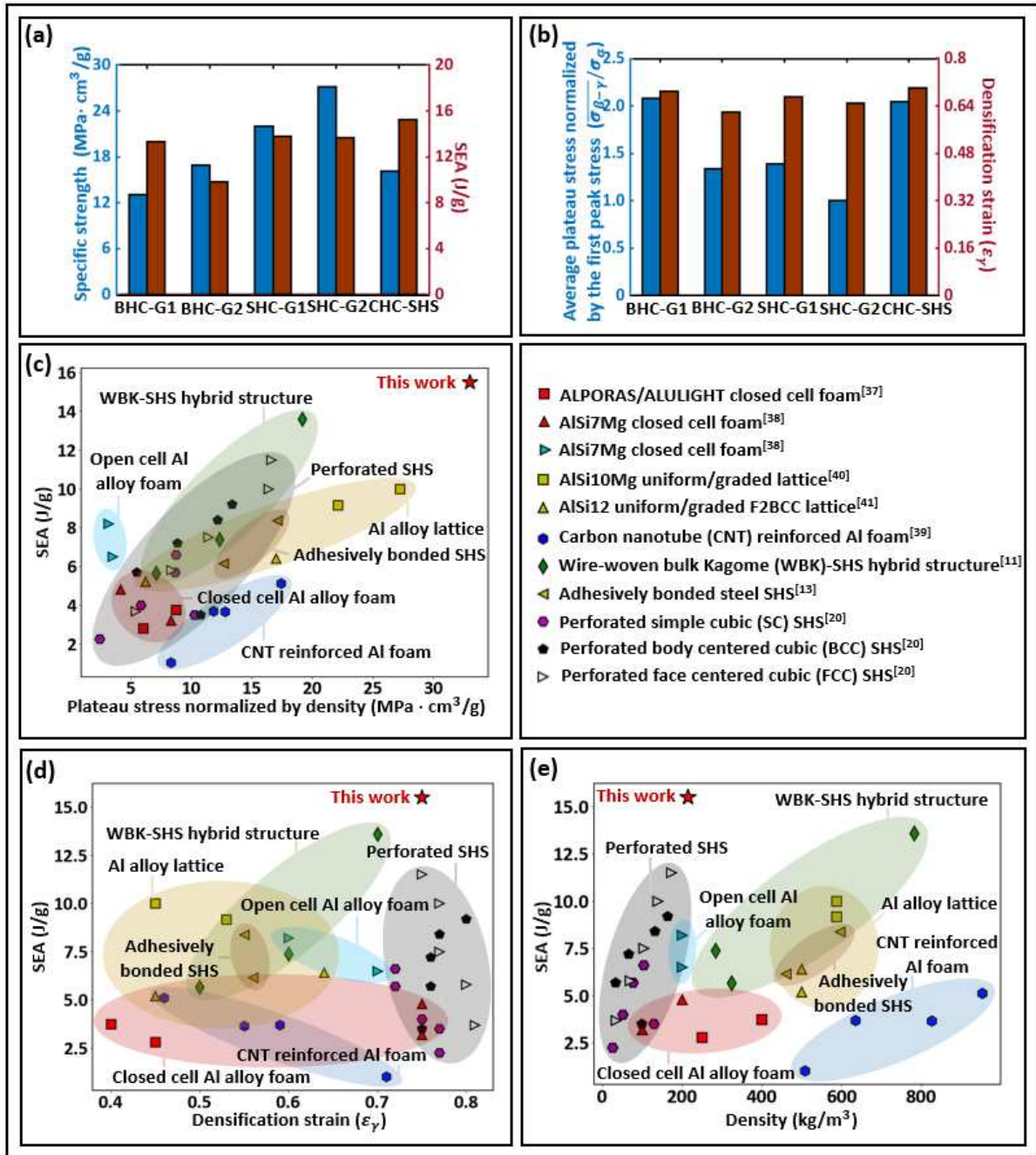


**Figure 2.** Material property comparison of the BHC-G1/2, SHC-G1/2, and CHC-SHS lattice structures and recently published lightweight structures: (a-b) summaries of normalized average plateau stress, densification strain, specific strength, and specific energy absorption of the BHC-G1/2, SHC-G1/2, and CHC-SHS lattice structures; (c-e) Ashby charts reflecting the SEA, density-normalized plateau stress, densification strain, and density of lightweight structures including aluminum alloy foams<sup>[26-29]</sup>, aluminum alloy lattice structures<sup>[30]</sup>, different designs of SHS<sup>[11, 13, 20]</sup>, and the CHC-SHS cell designed in this work.

## Discussion

In summary, this study provided a biometric hierarchical SHS design and a multilevel failure mode engineering strategy, in which a composite hierarchical SHS lattice structure was developed with excellent SEA, deformation capability, and plateau stress magnitude. To

artificially control the mechanical properties of the BH-SHS unit cells and engineer the distribution of the mechanical properties of the BH-SHS lattice structures, compressive experiments were conducted to study the relationships between the microstructural topology type, topological density, and the corresponding mechanical properties of the BH-SHS unit cells. According to the established mathematical models, a multilevel failure mode engineering strategy was achieved by artificially distributing BH-SHS unit cells within the pixelized design space of the desired failure factors. In this paper, engineering examples were provided to demonstrate the potential applications of the proposed failure mode engineering method in the aerospace industry. To further validate the effectiveness of the proposed bio-inspired hierarchical design and multilevel failure mode engineering method, a novel CHC-SHS lattice structure was developed using a combination of bio-inspired laminated failure mode and crystal-inspired grain boundary hardening mechanisms, wherein the gradient of the CHC-SHS was optimized based on experimental studies of the BHC-G1/2 and SHC G1/2 lattice structures. Based on the investigation of the compressive behavior of CHC-SHS, the following conclusions were drawn:

(1) The compressive stress–strain curves of the BHC-G1/2, SHC-G1/2, and CHC-SHS lattice structures were composed of three stages: (a) wavy stage, (b) climbing plateau stage, and (c) densification stage. With the same topological design of the BH-SHS unit cells, the lattice structure with a higher  $\sigma_{If}(N)$  gradient level was observed to exhibit greater  $\varepsilon_\gamma$  and SEA values, which was due to a reduced number of stage overlaps among the lattice regions with adjacent failure levels.

(2) Compared with the BHC-G1/2 and SHC-G1/2, CHC-SHS possessed a further delayed densification stage. This was due to the fact that the CHC-SHS was designed with a combination of two types of unit cell topologies with distinguishing laminated failure levels, wherein the number of the pre-engineered failure stages was tremendously increased.

(3) The deformation of the unit cells for the CHC-SHS was effectively constrained by the intensively engineered crystal-inspired grain boundaries. This hardening strategy resulted in a shifted failure sequence for the SHC-SHS unit cells; hence, an improved magnitude of the climbing plateau stage for its stress–strain curve.

(4) The direct comparison results between the CHC-SHS and recently reported lightweight structures, including aluminum lattices, aluminum foams, and different SHS designs, revealed that the CHC-SHS proposed in this work possessed higher SEA, deformation capability, and plateau magnitude. These advantages demonstrate the applicability of CHC-SHS in lightweight energy absorption systems such as protective aerospace components.

This work inspires three research directions. First, the mechanical effects of surface topologies other than honeycomb can be studied for SHS lattice structures. Second, because the proposed failure mode engineering method is not limited to SHS lattice structures, it can be applied for other types of surface-dominated lattice structures such as the triply periodic minimal surface lattice. Finally, more bio-inspired toughening mechanisms can be studied and achieved on the basis of the microstructural-failure-mode-design method proposed in this paper.

## **Methods**

**Design of BH-SHS unit cell.** The procedure for designing a BH-SHS unit cell can be generally divided into three processes: (1) the generation of the surface of a pure SHS unit cell; (2) the development of a biomimetic hierarchical (BH) cutting wireframe; and (3) the Boolean operation between the surface of the pure SHS unit cell and BH cutting wireframe. The detailed design flow is shown in Figure 3. In this study, the honeycomb structure was applied as the hierarchical design of the surface topology of BH-SHS owing to its enhanced mechanical energy absorption properties<sup>[8, 31, 32]</sup>, wherein a bending-dominated honeycomb SHS (BHC-SHS) and a stretch-dominated honeycomb SHS (SHC-SHS) were selected so that different compressive failure mechanisms could be achieved.

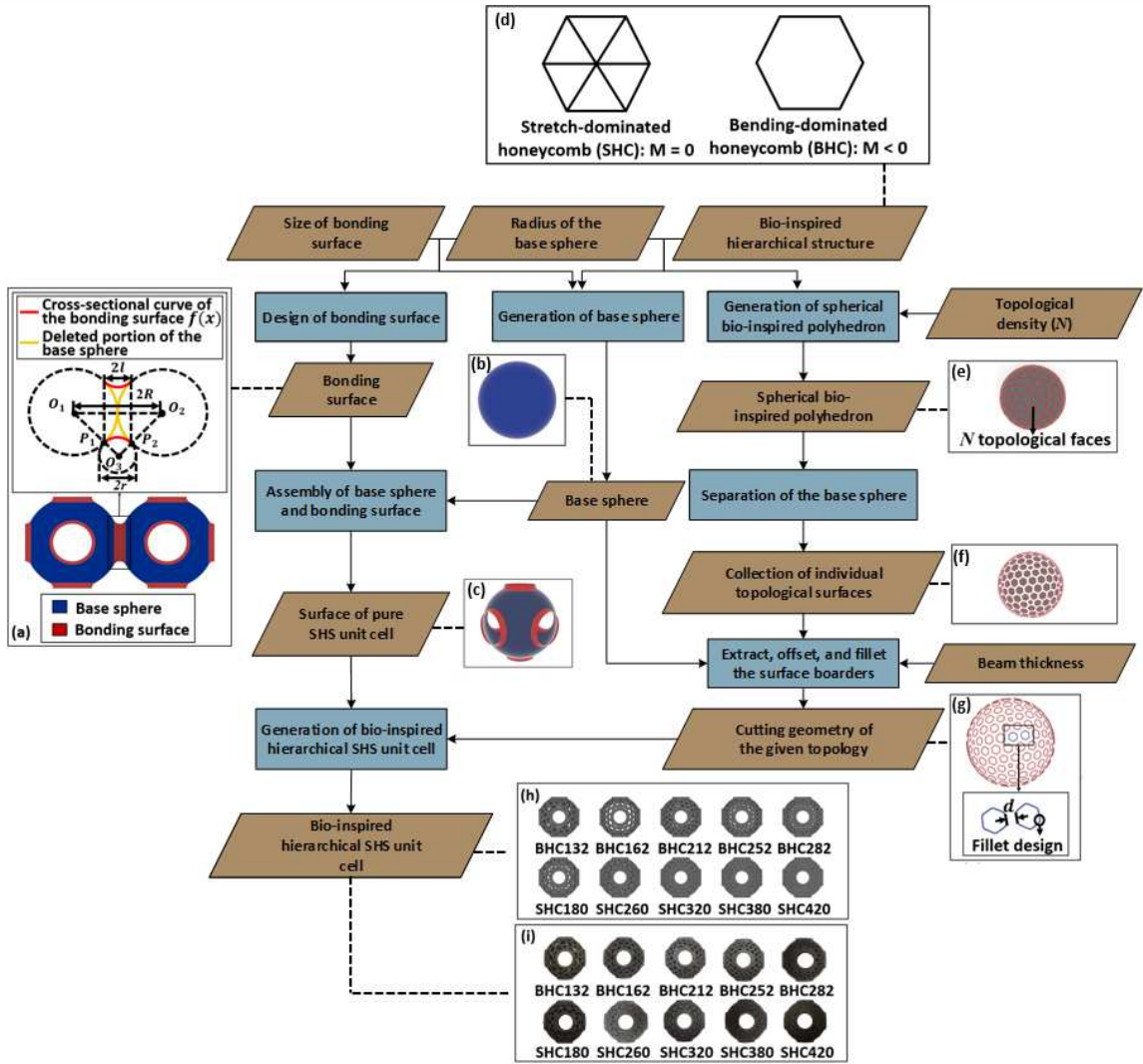


**Figure 3.** General workflow of BH-SHS lattice unit cells: (a) bonding surface design; (b) base sphere; (c) surface of pure SHS unit cell; (d) bio-inspired hierarchical structure; (e) spherical biometric polyhedron; (f) individual topological surfaces; (g) cutting wireframe; (h) BH-SHS unit cells designed with different topological densities; and (i) experimentally fabricated BH-SHS unit cells.

The surface of a pure SHS unit cell is developed on the basis of the Boolean assembly of the bonding surfaces and base sphere, as shown in Figure 3a-c, wherein size of the bonding surface  $l$  and radius of the base sphere  $R$  are required. To design the geometry of the bonding surface, the related design parameters are restricted based on Equations 1 and 2 to reduce the stress concentrations between adjacent SHS unit cells:

$$\frac{R+r}{R} = \frac{R}{R-l} \quad (1)$$

$$k_{P_i} = \frac{f''(x_{P_i})}{(1+(f'(x_{P_i}))^2)^{\frac{3}{2}}} = 0 \quad (2)$$

where  $r$  is the radius of the circle  $O_3$  tangent to the cross-sectional curve of the bonding surface,  $P_i$  represents the tangential points between the bonding surface and the base sphere,  $f(x)$  describes the cross-sectional curve of the bonding surface, and  $k_{P_i}$  calculates the curvature of  $f(x)$  at  $P_i$ .

To develop the cutting wireframe for pure SHS unit cells, three subprocesses were performed: (1) the generation of the spherical bio-inspired polyhedron, (2) the separation of the base sphere, and (3) the extraction, offset, and fillet operation of the borders for individual topological surfaces. An open-source plug-in named Polyhedron is utilized in Rhino 6 to obtain the BHC and SHC polyhedra; the edges of these polyhedra are offset and sphericalized to the base sphere, as shown in Figure 3e. Note that the topological density of a polyhedron was represented by the total number of its topological faces  $N$ . To derive the cutting geometry, the base sphere is divided into individual topological surfaces based on the spherical polyhedron wireframe provided in Figure 3f. Subsequently, the border of each individual topological surface is extracted and offset toward its geometrical center with half of beam thickness  $d$ , as shown in Figure 3g, wherein the offset wireframe is also tailored with filleted corners to decrease the stress concentrations within the structures of the BH-SHS unit cells.

Once the surface of the pure SHS unit cell and the geometry of the BH cutting wireframe were generated, Boolean operations could be performed to form the BH-SHS unit cells. The surface of the BH-SHS unit cell was created by removing the topological patterns that were separated by the cutting wireframe, and the solidified BH-SHS unit cells were developed by offsetting this surface with shell thickness  $t$ . In this study, two types of BH-SHS unit cells were designed and fabricated with SHC and BHC surface topologies shown in Figure 3h-i. For each unit cell topology, five different topological densities were developed. Table S1 summarizes the design parameters of the BH-SHS unit cells, wherein the beam thickness, the shell thickness, and the lower limits of the topological densities were determined on the basis of the balance

achieved by offering the smallest relative density while maintaining a good geometrical agreement between the CAD design and fabrication results of the BH-SHS unit cells.

**Mechanical modeling of BH-SHS unit cells.** In this study, the BH-SHS unit cells were manufactured using the SLM technique; the detailed information on the building platform and the process parameters are listed in Table 1. The AlMgScZr powder, as shown in Figure 4a, was selected as the building material. The material composition of the powder is summarized in Figure S1. The scanning electron microscope (SEM) images of the elementary distributions of the powder are shown in Figure S1. The mechanical properties of the as-built AlMgScZr alloys were obtained through tensile tests based on the ASTM E8 standard, and revealed that the as-built AlMgScZr alloy possessed an average modulus of 75 GPa, yield stress of 366 MPa, ultimate stress of 422 MPa, and fracture strain of 19%. The standard deviations of the mechanical properties of the specimens are provided in Table 2, wherein good consistency of the mechanical performance is observed among the printed samples. The detailed dimensions of the specimens are provided in Table S3.

**Table 1.** Building platform and process parameters of the SLM procedure.

Building platform	EOS M280 SLM printer
Layer thickness [ $\mu\text{m}$ ]	30
Hatch distance [ $\mu\text{m}$ ]	80
Laser speed [mm/s]	1600
Laser power [W]	370
Beam offset [ $\mu\text{m}$ ]	20
Stripe width [mm]	5
Overlap [ $\mu\text{m}$ ]	50

To study the compressive characteristics of the BH-SHS unit cells and to model their mechanical properties based on the topological types and densities, compressive experiments and simulations were performed. The detailed recordings of the simulations are given in Video S1 and Video S2. During the compressive process, the compression rate was set to 2 mm/min to satisfy the quasi-static condition of the compression, wherein each unit cell was compressed

beyond its densification stage. To improve the accuracy of the simulation, the structural dimensions of the as-built BH-SHS unit cells were measured using an optical microscope and compared with the original designs. For each BH-SHS unit cell, measurements were performed for a representative unit area with a full range of beam angles, as shown in Figure S2a, with the measurement results summarized in Figure S2b. This indicated that the actual beam thicknesses of the BH-SHS unit cells ranged from 887  $\mu\text{m}$  to 1055  $\mu\text{m}$ , which was offset  $-113 \mu\text{m}$  to  $+55 \mu\text{m}$  from the designed value, while the shell thicknesses of BH-SHS unit cells was offset approximately  $-100 \mu\text{m}$  to  $-200 \mu\text{m}$  from the original designs. As reported in previous studies<sup>[33-35]</sup>, numerous factors related to the SLM process can potentially cause geometrical variations, such as partially melted metal particles and large overhanging angles. These flaws were typically related to the nature of the SLM process and led to a reduction in the geometrical accuracy and mechanical properties of the built materials. Thus, the simulation models of the BH-SHS unit cells were corrected based on the experimental observations of the beam and shell thickness to provide a more accurate prediction of the stress distribution of the BH-SHS unit cells during the compression tests.

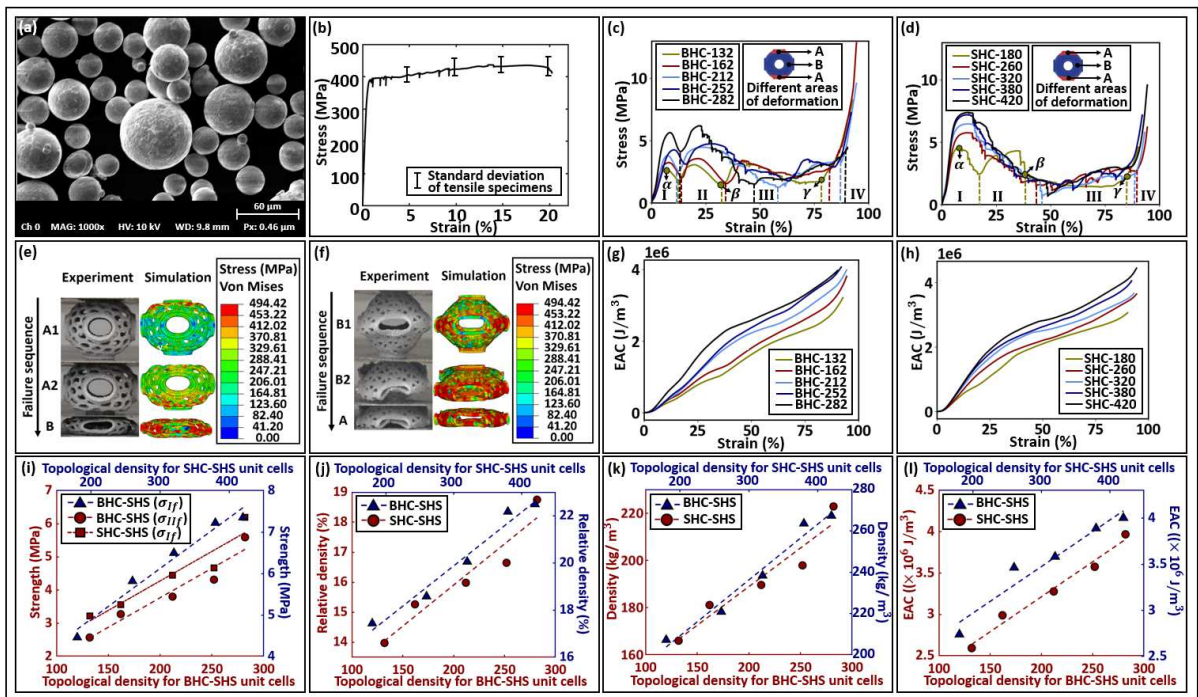


**Figure 4.** Material property and mechanical modeling of BH-SHS unit cells: (a) SEM image of AlMgScZr powder; (b) stress–strain curve for the SLM AlMgScZr alloy; (c-d) simulation and

experimental stress–strain curve for BHC-SHS and SHC-SHS unit cells; (e-f) experimental and simulational failure analysis of BHC-SHS and SHC-SHS unit cells; (g-h) EAC with different strain values for BHC-SHS and SHC-SHS unit cells; and (i-l) relationship among the compressive strength, relative density, density, EAC, and topological density for BHC-SHS and SHC-SHS unit cells.

**Table 2.** Summary and standard deviation of the mechanical properties of SLM as-built AlMgScZr.

Specimen #	1	2	3	Average	Standard deviation
Modulus [GPa]	81	72	72	75	5.2
Yield stress [MPa]	380	364	355	366	12.7
Ultimate stress [MPa]	437	417	412	422	13.2
Maximum elongation [%]	20	19	17	19	1.5

Figure 4c-d provides the experimental stress–strain curves of the BHC-SHS and SHC-SHS unit cells with different topological densities. Compared with the experimental results, a slightly postponed fracture is observed in the simulations, as shown in Figure 4e-f. This is due to the intrinsic SLM defects of the as-built BH-SHS unit cells, such as pores, voids, and powder adhesion<sup>[36, 37]</sup>, which also resulted in the observation of a rough surface finish, as shown in Figure S3 and Figure S4. These defects caused a higher stress concentration and, hence, an earlier plastic deformation of the structures and reduced mechanical performance. Combining the experimental stress–strain curves with the simulated failure sequence and the stress distribution results, the compressive process of the BHC-SHS and SHC180 unit cells could be characterized into four stages:

- I: The first wavy stage, wherein one of the top/bottom areas (A) collapsed.
- II: The secondary wavy stage, which corresponded to the collapse of the top/bottom area (A) that persisted in stage I, and the post-collapse deformation of the regions that were deformed at stage I.
- III: The plateau stage, wherein plastic deformation occurred in the middle area (B).
- IV: The densification stage, wherein the entire structure of the unit cells was forced to contract.

For the SHC260 to SHC420 unit cells, different characterization of the failure sequence was observed:

- I-II: The wavy stage, wherein the middle area (B) collapsed.
- III: The plateau stage, which corresponded to the continuous collapse and fracture of the middle area (B).
- IV: The densification stage, wherein both the top and bottom areas (A) failed, and the entire structure of the unit cells was forced to contract.

Owing to the distinct failure sequences, large variations in strain limits and the relative stress magnitudes of each compressive stage were observed between the BHC-SHS and SHC-SHS unit cells. To illustrate, the upper range of the wavy strain for the SHC-SHS unit cells was approximately 55%–60%, which was significantly broader than the approximately 30%–35% for the BHC-SHS unit cells. Moreover, the plateau stage of the BHC-SHS unit cells accounted for approximately 70% of the total strain, which was twice the value for the SHC-SHS unit cells (35%). To compare the relative magnitude of the compressive plateau, the normalized average plateau stresses were calculated using Equation (1):

$$\sigma_{NP} = \frac{\int_{\varepsilon_{\beta}}^{\varepsilon_{\gamma}} \sigma d\varepsilon}{\sigma_{\alpha}} \quad (1)$$

where  $\sigma_{NP}$  is the normalized average plateau stress,  $\sigma_{\alpha}$  is the peak stress at stage I,  $\varepsilon_{\beta}$  and  $\varepsilon_{\gamma}$  represent the strain limits of the plateau stage. Compared to the BHC-SHS unit cells that exhibit 1.45–1.52 MPa/MPa normalized average plateau stress, the SHC-SHS unit cells were observed to possess a lower normalized average plateau stress, ranging from 0.34 MPa/MPa to 0.49 MPa/MPa. To further analyze the energy absorption behaviors of the BHC-SHS and SHC-SHS unit cells, the EAC was calculated for each strain value based on Equation (2):

$$EAC(\varepsilon_A) = \frac{\int_0^{\varepsilon_A} \sigma(\varepsilon) d\varepsilon}{V_{sphere}} \quad (2)$$

where  $EAC(\varepsilon_A)$  represents the EAC at strain  $\varepsilon_A$  and  $V_{sphere}$  is the volume of the unit cell. The results of the calculations for the BHC-SHS and SHC-SHS unit cells are provided in Figure 4g-h. It was found that the EAC of the BHC-SHS unit cells showed a more significant increase at the plateau stage, while the SHC-SHS unit cells absorbed more energy at the wavy stage. Compared to the SHC-SHS unit cells, the BHC-SHS unit cells showed a higher normalized plateau stress and a longer plateau stage. Overall, the SHC-SHS unit cells exhibited higher stiffness and strength values, while the BHC-SHS unit cells were ideal energy absorbers to protect more fragile components that cannot suffer high stresses in the wavy stage. The distinctive ranges of the compressive stages and the different quantities of energy absorbed at these stages between the BHC-SHS and SHC-SHS unit cells also allowed for designing BH-SHS lattices with composite failure mechanisms achieved by an effective combination of these topologies.

The derived relationships between the topological density, relative density, density, compressive strength, and total EAC of the BHC-SHS and SHC-SHS unit cells are shown in Figure 4i-l. Specifically, relative density of the unit cells  $RD$  was calculated by dividing structural volume of the unit cell  $V_{struct}$  by total volume of the unit cell cubic  $V_{cubic}$  as shown in Equation (3):

$$RD = \frac{V_{struct}}{V_{cubic}} \quad (3)$$

In addition, the compressive wavy strength at stages I and II was defined as the maximum compressive stress within the range of those stages. The total EAC was calculated as the energy absorbed per unit volume of the structure until its densification strain as shown in Equation (4):

$$EAC_T = \frac{\int_0^{\varepsilon_\gamma} \sigma d\varepsilon}{V_{sphere}} \quad (4)$$

where  $\varepsilon_\gamma$  is the densification strain and  $EAC_T$  is the total EAC. Based on these theoretical calculations and experimental results, the following mechanical models were established:

$$RD(N, T) = A_{RD}(T)N - B_{RD}(T, N) \quad (5)$$

$$\rho(N, T) = A_{\rho}(T)N + B_{\rho}(T, N) \quad (6)$$

$$\sigma_{I_f}(N, T) = A_{\sigma_{I_f}}(T)N + B_{\sigma_{I_f}}(T) \quad (7)$$

$$\sigma_{II_f}(N, T) = A_{\sigma_{II_f}}(T)N + B_{\sigma_{II_f}}(T) \quad (8)$$

$$EAC(N, T) = A_{EAC}(T)N + B_{EAC}(T) \quad (9)$$

where the topological density of a unit cell is represented by number of individual topological surfaces  $N$ ,  $T$  represents the type of the surface topology,  $RD$  is the relative density of the unit cell,  $\sigma_{I_f}$  is the strength of stage I,  $\sigma_{II_f}$  is the strength of stage II, and  $EAC(N, T)$  is the EAC of the unit cell with topology type  $T$  and topological density  $N$ . The values of positional parameters  $A$  and  $B$  are summarized in Table 3, wherein the values of  $B_{RD}$ ,  $B_{\rho}$ ,  $B_{\sigma}$ , and  $B_{EAC}$  are calculated on the basis of the unit systems of % for relative density,  $\text{kg/m}^3$  for density, MPa for strength, and  $\text{J/m}^3$  for EAC, respectively. Based on these models, a theoretical design guideline was established to facilitate artificial engineering of a preferred distribution of mechanical properties of the unit cells within the design space.

**Table 3.** Summary of the positional parameters for the mechanical models of BH-SHS unit cells.

Topology type	BHC	SHC
$A_{RD}$	$2.74 \times 10^{-2}$	$2.28 \times 10^{-2}$
$A_{\rho}$	$3.27 \times 10^{-1}$	$2.70 \times 10^{-1}$
$A_{\sigma_{I_f}}$	$1.78 \times 10^{-2}$	$1.22 \times 10^{-2}$
$A_{\sigma_{II_f}}$	$1.78 \times 10^{-2}$	NA
$A_{EAC}$	$8.46 \times 10^3$	$5.03 \times 10^3$
$B_{RD}$	$1.04 \times 10^1$	$1.30 \times 10^1$
$B_{\rho}$	$1.52 \times 10^6$	$1.55 \times 10^2$
$B_{\sigma_{I_f}}$	$2.12 \times 10^{-1}$	2.46
$B_{\sigma_{II_f}}$	$7.23 \times 10^{-1}$	NA
$B_{EAC}$	$1.52 \times 10^6$	$1.96 \times 10^6$

**Multilevel failure mode engineering.** Based on the derived mechanical models of the BH-SHS unit cells, a multilevel failure mode engineering strategy was proposed. To illustrate this,

failure propagation is artificially tailored through the multilevel design of the failure sequences, as shown in Figure 5a. Specifically, the provided design space was first pixelized with size  $S$  identical to the cubic dimensions of the BH-SHS unit cells, wherein the failure sequence of each pixel was represented by failure factor  $F(x, y, z)$  ranging from  $F_1$  to  $F_N$ . This failure factor was calculated as the safety level that indicated the extent to which each BH-SHS unit cell pixel could move prior to its collapse, and the condition in Equation (10) needed to be met to guarantee the correct failure sequence:

$$F_i < F_{i+1}, i = 1, \dots, N - 1 \quad (10)$$

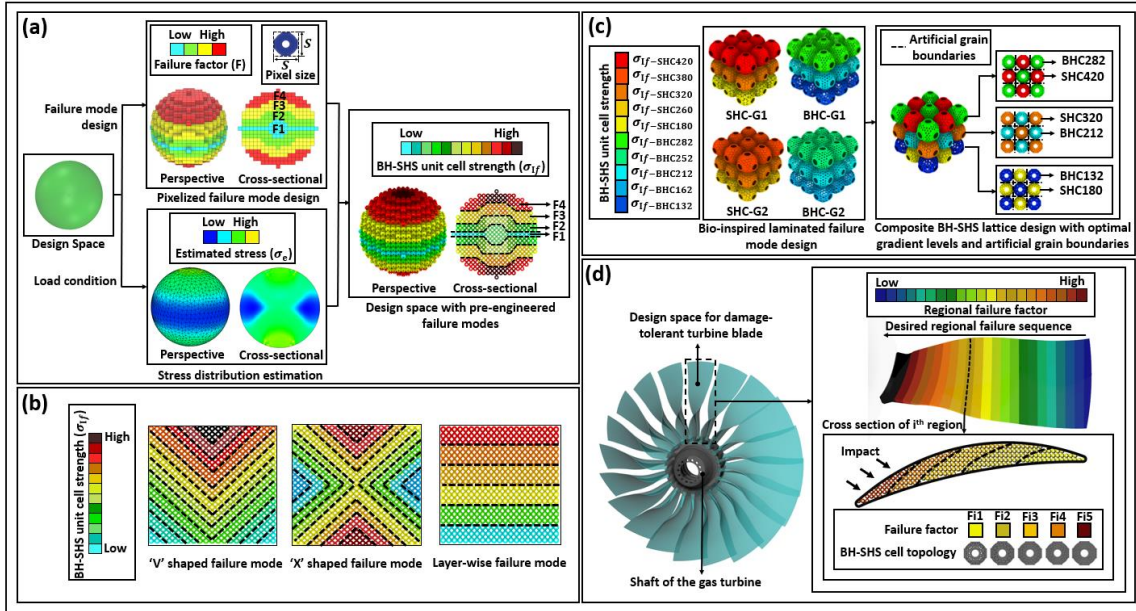


**Figure 5.** Diagrams of the multilevel failure mode engineering method, typical failure mode designs, and high-energy-absorption composite BH-SHS lattice design: (a) multilevel failure mode engineering method; (b) different typical shapes of failure modes; (c) gradient design of composite BH-SHS lattice structure with crystal-inspired grain boundaries; and (d) a lightweight damage-tolerant turbine blade design with composite BH-SHS lattice infills.

Moreover, the stress distribution in the design space was estimated on the basis of the actual load requirements. According to the definition of the failure factor and the estimated stress distribution of the design space, the strengths of stages I and II for the BH-SHS unit cell at a certain pixel position  $(x, y, z)$  can be derived from Equations (11) to (12):

$$\sigma_{If}(x, y, z) = F(x, y, z)\sigma_e(x, y, z) \quad (11)$$

$$\sigma_{II f}(x, y, z) = W(x, y, z)\sigma_e(x, y, z) \quad (12)$$

where  $F(x, y, z)$  is the pre-designed failure factor,  $W(x, y, z)$  represents the safety factor of the secondary wavy stage, and  $\sigma_e(x, y, z)$  is the estimated stress located at  $(x, y, z)$ . For adjacent failure levels, Equation (13) should be satisfied to avoid the simultaneous collapse of the wavy stages of their unit cells:

$$W(x_i, y_i, z_i) < F(x_{i+1}, y_{i+1}, z_{i+1}), i = 1, \dots, N - 1 \quad (13)$$

where  $(x_i, y_i, z_i)$  represents the coordinates of the pixel located at failure level  $i$  with failure factor  $F_i$ . Combining the results from Equations (7), (8), and (13), the relationship between the wavy strength and topological density of the BH-SHS unit cells at adjacent failure levels is established in Equations (14) and (15):

$$\frac{\sigma_{II_f}(x_i, y_i, z_i)}{\sigma_{I_f}(x_{i+1}, y_{i+1}, z_{i+1})} < C_{i,i+1} \quad (14)$$

$$A_{\sigma_{I_f}}(T(x_i, y_i, z_i))N(x_i, y_i, z_i) - C_{i,i+1}A_{\sigma_{II_f}}(T(x_{i+1}, y_{i+1}, z_{i+1}))N(x_{i+1}, y_{i+1}, z_{i+1}) < C_{i,i+1}B_{\sigma_{II_f}}(T(x_{i+1}, y_{i+1}, z_{i+1})) - B_{\sigma_{I_f}}(T(x_i, y_i, z_i)) \quad (15)$$

where  $C_{A,B} = \frac{\sigma_e(x_A, y_A, z_A)}{\sigma_e(x_B, y_B, z_B)}$  represents the ratio of the estimated stress located in regions A and

B. With these conditions satisfied, the structures within the design space would deform and collapse with a pre-engineered failure sequence. Moreover, typical failure modes, including “V” shaped, “X” shaped, and layer-wise failure shapes, as shown in Figure 5b, can be easily developed by the proposed method. According to previous research<sup>[3, 38-41]</sup>, composite structures with laminated combinations of mechanical properties are widely found in nature, and many promoted mechanical properties, such as crack deflection, high energy absorption, and high impact resistance. Furthermore, a layer-wise gradient design of the mechanical properties allowed the structure to exhibit moderate failure and a long stress plateau without undergoing a catastrophic structural collapse while also avoiding a decrease in stress during the compressive process, thereby producing a higher SEA. Therefore, a multilevel laminated failure mode was proposed to develop a composite BH-SHS lattice structure with improved

SEA, shown in Figure 5c. To study the effect of the gradients for stage I strength  $\sigma_{If}(N)$  of both SHC-SHS and BHC-SHS lattice structures with an artificially engineered layer-wise failure mode on their compressive energy absorption behaviors, two levels of  $\sigma_{If}(N)$  gradients were designed on the basis of the proposed mechanical models of the BH-SHS unit cells. To further improve the energy absorption performance of the BH-SHS lattice structure, a composite honeycomb SHS (CHC-SHS) lattice with multi-failure modes was developed using a combination of the crystal-inspired hardening mechanism and the layer-wise failure mode. For the composition of the CHC-SHS lattice structure, both SHC-SHS and BHC-SHS unit cells were layer-wise distributed with an optimal  $\sigma_{If}(N)$  gradient, wherein a hardening grain boundary design pattern was included within each layer of the lattice. This multilevel failure mode design was expected to offer a longer plateau to the CHC-SHS lattice structure with an increased number of failure levels, which were enabled by the distinctive failure mechanisms of different topological designs of the BH-SHS unit cells. In addition, the artificial grain boundaries could potentially improve the relative magnitude of the stress plateau of the lattice structure by constraining the effect of the unit cells with different topologies. Figure 5d shows a case study of applying the BH-SHS unit cells as protective infills for an aerospace turbine blade. In this case study, the failure mode of the turbine blade was artificially engineered to resist the potential impact and protect its shaft from the disintegrated turbine fragments. To illustrate the generality of the proposed method, additional application examples, including a damage-deflective wheel for the space rover and a protective structural infill for a quadradrone, are provided in Figure S5.

## References

- [1] J. Mueller, J. R. Raney, K. Shea, J. A. Lewis, *Advanced Materials* 2018, 30, 1705001.
- [2] S. Babae, J. Shim, J. C. Weaver, E. R. Chen, N. Patel, K. Bertoldi, *Advanced Materials* 2013, 25, 5044.
- [3] Z. Gao, D. Li, G. Dong, Y. F. Zhao, *Additive Manufacturing* 2020, 36, 101539.
- [4] S. Sadeghzade, R. Emadi, M. Salehi, F. Tavangarian, A. Ramini, *Theoretical and Applied Fracture Mechanics* 2020, 110, 102797.

- [5] M.-S. Pham, C. Liu, I. Todd, J. Lertthanasarn, *Nature* 2019, 565, 305.
- [6] Y. Chen, L. Wang, *Scientific reports* 2015, 5, 17865.
- [7] J. Song, W. Zhou, Y. Wang, R. Fan, Y. Wang, J. Chen, Y. Lu, L. Li, *Materials & Design* 2019, 173, 107773.
- [8] J. Xiang, J. Du, *Materials Science and Engineering: A* 2017, 696, 283.
- [9] Z. Y. Gao, T. X. Yu, H. Zhao, *Journal of Aerospace Engineering* 2008, 21, 206.
- [10] C. Jsab, B. Dh, C. Sl, A. Wl, C. Dw, A. Qs, C. Gz, *Engineering Structures*, 226.
- [11] Y. Stylianos, M. Orestes, R. A. Votsis, F. P. Brennan, *Mechanics Research Communications* 2018, S0093641318301587.
- [12] T. X. Yu, D. Karagiozova, Z. Y. Gao, "The Dependence of the Energy-absorption Capacity of Metal Hollow Sphere Materials on Their Relative Density", presented at *Engineering Plasticity and Its Applications from Nanoscale to Macroscale pt.1; Key Engineering Materials; vol.340-341*, 2007.
- [13] M. Z. Li, G. Stephani, K. J. Kang, *Advanced Engineering Materials* 2011, 13, 33.
- [14] Joseph, A., Santa, Maria, Benjamin, F., Schultz, J., B., Ferguson, *Journal of Materials Science* 2014.
- [15] Y. Liu, H. X. Wu, G. Lu, B. Wang, *Mechanics of Composite Materials & Structures* 2013, 20, 478.
- [16] A. Rabiei, L. Vendra, *Materials Letters* 2009, 63, 533.
- [17] S. Yiatros, O. Marangos, R. A. Votsis, F. P. Brennan, *Mechanics Research Communications* 2018, 94, 13.
- [18] A. Nazir, K. M. Abate, A. Kumar, J.-Y. Jeng, *The International Journal of Advanced Manufacturing Technology* 2019, 104, 3489.
- [19] S. Yuan, C. K. Chua, K. Zhou, *Advanced Materials Technologies* 2019, 4, 1800419.
- [20] M. Dai, J. Liang, C. Cheng, Z. Wu, J. Lu, J. Deng, *Materials* 2021, 14, 3716.
- [21] S. M. Sajadi, L. Vásárhelyi, R. Mousavi, A. H. Rahmati, Z. Kónya, Á. Kukovecz, T. Arif, T. Filleter, R. Vajtai, P. Boul, *Science Advances* 2021, 7, eabc5028.
- [22] R. Manno, W. Gao, I. Benedetti, *Extreme Mechanics Letters* 2019, 26, 8.
- [23] G. X. Gu, F. Libonati, S. Wettermark, M. J. Buehler, *J Mech Behav Biomed Mater* 2017, S1751616117301959.
- [24] G. X. Gu, M. Takaffoli, A. J. Hsieh, M. J. Buehler, *Extreme Mechanics Letters* 2016, 317.
- [25] L. R. Meza, A. J. Zelhofer, N. Clarke, A. J. Mateos, J. R. Greer, *Proceedings of the National Academy of Sciences of the United States of America* 2015, 112.
- [26] M. Idris, T. Vodenitcharova, M. Hoffman, *Materials Science and Engineering: A* 2009, 517, 37.
- [27] A. Jung, H. Natter, S. Diebels, E. Lach, R. Hempelmann, *Advanced Engineering Materials* 2011, 13, 23.
- [28] I. Maskery, N. Aboulkhair, A. Aremu, C. Tuck, I. Ashcroft, R. D. Wildman, R. Hague, *Materials Science and Engineering: A* 2016, 670, 264.
- [29] A. Aldoshan, S. Khanna, *Materials Science and Engineering: A* 2017, 689, 17.
- [30] D. S. Al-Saedi, S. Masood, M. Faizan-Ur-Rab, A. Alomarah, P. Ponnusamy, *Materials & Design* 2018, 144, 32.
- [31] I. Q. Alonso, N. J. S. M. Fleck, 2007, 56, 693.
- [32] J. Huang, L. J. A. m. e. m. Gibson, 1991, 39, 1617.
- [33] H. Gong, K. Rafi, T. Starr, B. Stucker, "Effect of defects on fatigue tests of as-built Ti-6Al-4V parts fabricated by selective laser melting", presented at *Solid freeform fabrication symposium*, 2012.
- [34] T. Maconachie, M. Leary, B. Lozanovski, X. Zhang, M. Qian, O. Faruque, M. Brandt, *Materials & Design* 2019, 108137.

- [35] E. O. Olakanmi, R. Cochrane, K. Dalgarno, *Progress in Materials Science* 2015, 74, 401.
- [36] S. Tammam-Williams, H. Zhao, F. Léonard, F. Derguti, I. Todd, P. B. Prangnell, *Materials Characterization* 2015, 102, 47.
- [37] S. L. Sing, W. Y. Yeong, F. E. Wiria, B. J. E. M. Tay, 2016, 56, 735.
- [38] L. Ying, H. X. Wu, B. Wang, *Composites Part B* 2012, 43, 1346.
- [39] A. Mao, N. Zhao, Y. Liang, H. Bai, *Advanced Materials* 2021, 33, 2007348.
- [40] K. J. Koester, J. Ager, R. Ritchie, *Nature materials* 2008, 7, 672.
- [41] L. O. Jernkvist, Luleå tekniska universitet, 2000.

## Supplementary Files

This is a list of supplementary files associated with this preprint. Click to download.

- [3368340supp5992233r1b3lm.docx](#)
- [Supportingvideos.zip](#)